Observation of Two-Neutrino Double-Beta Decay in ^{136}Xe with the EXO-200 Detector

N. Ackerman,[1,*] B. Aharmim,[2] M. Auger,[3] D. J. Auty,[4] P. S. Barbeau,[5,†] K. Barry,[5] L. Bartoszek,[5] E. Beauchamp,[2] V. Belov,[6] C. Benitez-Medina,[7] M. Breidenbach,[1] A. Burenkov,[6] B. Cleveland,[2] R. Conley,[1] E. Conti,[1,‡] J. Cook,[8] S. Cook,[7] A. Coppens,[9] I. Counts,[5] W. Craddock,[1] T. Daniels,[8] M. V. Danilov,[6] C. G. Davis,[10] J. Davis,[5] R. deVoe,[5] Z. Djurcic,[4,§] A. Dobi,[10] A. G. Dolgolenko,[6] M. J. Dolinski,[5] K. Donato,[2] M. Dunford,[9] W. Fairbank, Jr.,[7] J. Farine,[2] P. Fierlinger,[11] D. Franco,[3] D. Freytag,[1] G. Giroux,[3] R. Gornea,[3] K. Graham,[9] G. Gratta,[5] M. P. Green,[5] C. Hägemann,[9] C. Hall,[10] K. Hall,[7] G. Haller,[1] C. Hargrove,[9] R. Herbst,[1] S. Herrin,[1] J. Hodgson,[1] M. Hughes,[4] A. Johnson,[1] A. Karelin,[6] L. J. Kaufman,[12] T. Koffas,[5,‖] A. Kuchenkov,[6] A. Kumar,[5] K. S. Kumar,[8] D. S. Leonard,[13] F. Leonard,[9] F. LePort,[5,¶] D. Mackay,[1] R. MacLellan,[4] M. Marino,[11] Y. Martin,[3,**] B. Mong,[7] M. Montero Díez,[5] P. Morgan,[8] A. R. Müller,[5] R. Neilson,[5] R. Nelson,[14] A. Odian,[1] K. O'Sullivan,[5] C. Ouellet,[9] A. Piepke,[4] A. Pocar,[8] C. Y. Prescott,[1] K. Pushkin,[4] A. Rivas,[5] E. Rollin,[9] P. C. Rowson,[1] J. J. Russell,[1] A. Sabourov,[5] D. Sinclair,[9,††] K. Skarpaas,[1] S. Slutsky,[10] V. Stekhanov,[6] V. Strickland,[9,††] M. Swift,[1] D. Tosi,[5] K. Twelker,[5] P. Vogel,[15] J.-L. Vuilleumier,[3] J.-M. Vuilleumier,[3] A. Waite,[1] S. Waldman,[5,‡‡] T. Walton,[7] K. Wamba,[1] M. Weber,[3] U. Wichoski,[2] J. Wodin,[1] J. D. Wright,[8] L. Yang,[1] Y.-R. Yen,[10] and O. Ya. Zeldovich[6]

(EXO Collaboration)

[1]*SLAC National Accelerator Laboratory, Stanford, California, USA*
[2]*Physics Department, Laurentian University, Sudbury, Ontario, Canada*
[3]*LHEP, Albert Einstein Center, University of Bern, Bern, Switzerland*
[4]*Department of Physics and Astronomy, University of Alabama, Tuscaloosa, Alabama, USA*
[5]*Physics Department, Stanford University, Stanford, California, USA*
[6]*Institute for Theoretical and Experimental Physics, Moscow, Russia*
[7]*Physics Department, Colorado State University, Fort Collins, Colorado, USA*
[8]*Physics Department, University of Massachusetts, Amherst, Massachusetts, USA*
[9]*Physics Department, Carleton University, Ottawa, Ontario, Canada*
[10]*Physics Department, University of Maryland, College Park, Maryland, USA*
[11]*Technical University Munich, Munich, Germany*
[12]*Physics Department and CEEM, Indiana University, Bloomington, Indiana, USA*
[13]*Department of Physics, University of Seoul, Seoul, Korea*
[14]*Waste Isolation Pilot Plant, Carlsbad, New Mexico, USA*
[15]*Kellogg Lab, Caltech, Pasadena, California, USA*
(Received 21 August 2011; published 17 November 2011)

We report the observation of two-neutrino double-beta decay in ^{136}Xe with $T_{1/2} = 2.11 \pm 0.04(\text{stat}) \pm 0.21(\text{syst}) \times 10^{21}$ yr. This second-order process, predicted by the standard model, has been observed for several nuclei but not for ^{136}Xe. The observed decay rate provides new input to matrix element calculations and to the search for the more interesting neutrinoless double-beta decay, the most sensitive probe for the existence of Majorana particles and the measurement of the neutrino mass scale.

DOI: 10.1103/PhysRevLett.107.212501 PACS numbers: 23.40.−s, 14.60.Pq

Several even-even nuclei are stable against ordinary β decay but are unstable for $\beta\beta$ decay in which two neutrons are changed into two protons simultaneously. As is well known, $\beta\beta$ decay can proceed through several modes. The allowed process, the two-neutrino mode ($2\nu\beta\beta$), is completely described by known physics; its rate was first evaluated in Ref. [1]. Of the other, hypothetical, modes, the neutrinoless decay ($0\nu\beta\beta$) is forbidden in the standard model since it violates conservation of the total lepton number. Its observation would constitute proof that neutrinos are Majorana leptons [2], unlike all charged fermions that are of the Dirac type [3]. Moreover, the $0\nu\beta\beta$ decay can proceed only if neutrinos have mass [4]. Consequently, there is an intense worldwide program of experiments aiming at observing the $0\nu\beta\beta$ mode. The relation between the $0\nu\beta\beta$ half-life and the average Majorana neutrino mass requires the evaluation of nuclear matrix elements that, while different from those of the $2\nu\beta\beta$ decay mode, would benefit from their knowledge. Indeed, it has been suggested [5] that the theoretical parameters contributing to the largest uncertainties in the $0\nu\beta\beta$ matrix element calculation can be derived from the $2\nu\beta\beta$ decay matrix elements, known once the half-life has been experimentally measured. The half-life of the $2\nu\beta\beta$ decay depends on details of the nuclear structure that are known only approximately [6]. The $2\nu\beta\beta$ decay

has been observed in all important candidate nuclei [7] with one notable exception, ^{136}Xe, which until now had only lower limits on the half-life [8]. The most stringent published limit would imply a nuclear matrix element noticeably smaller than those found for other isotopes. From an experimental perspective, the $0\nu\beta\beta$ and $2\nu\beta\beta$ modes can be distinguished from the study of the energy spectrum of the electrons. The sum energy spectrum is a resolution-limited line at the Q value for $0\nu\beta\beta$ (2458 keV for ^{136}Xe [9]) and a broad continuum for $2\nu\beta\beta$, so that good energy resolution, along with the knowledge of the $2\nu\beta\beta$ rate, is essential in the search for $0\nu\beta\beta$.

The EXO-200 detector, shown in Fig. 1, is a time projection chamber (TPC) [10] using liquid Xe (LXe) as both the source of nuclear decays and the detection medium. The TPC has the geometry of a cylinder of 40 cm diameter and 44 cm length, with the drift field obtained by biasing a cathode grid dividing the cylinder into two identical regions. Each end of the cylinder is flared into a conical section, containing two wire grids and one array of ~250 large-area avalanche photodiodes (LAAPDs) [11] that allow for simultaneous readout of ionization and scintillation in the LXe. Wire grids cross at a 60° angle, providing two-dimensional localization and energy readout of each charge deposition. The third (longitudinal) coordinate is obtained from the time interval between the scintillation signal in the LAAPDs and the collection of the charge at the grids. A set of field-shaping rings, lined with reflective Teflon tiles, grades the field and limits the drift region to two cylinders, each of 18.3 cm radius and 19.2 cm length. For the data presented here the cathode bias was set to −8.0 kV, providing a field of 376 V/cm, designed to be uniform to within 1% over the entire fiducial volume. This low value of the electric field provides more stable operation at the expense of the ionization energy resolution that is not essential for the measurement of the $2\nu\beta\beta$ mode.

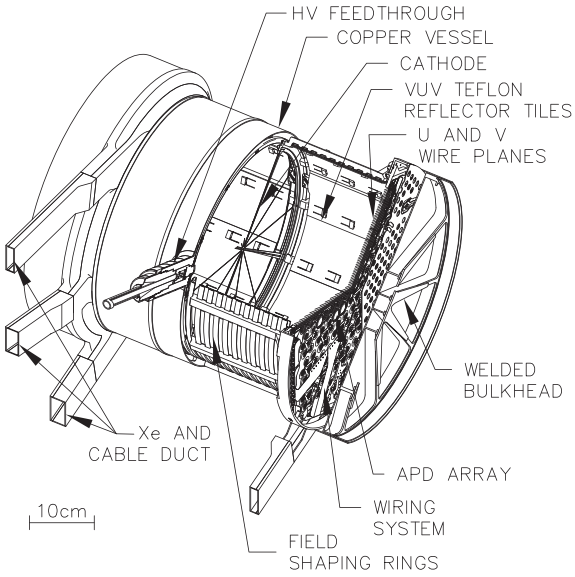

FIG. 1. Drawing of the EXO-200 TPC. The chamber contains ~175 kg of liquid xenon enriched to 80.6% in the isotope 136.

All components used for the construction of the detector were carefully selected for low radioactive content [12] and compatibility with electron drift in LXe. The TPC is mounted in the center of a low-background cryostat filled with ~2400 l of high-purity HFE7000 fluid [13] serving the purpose of innermost radiation shield and heat transfer fluid. At least 50 cm of HFE7000 (with a density of 1.8 g/cm^3 at 167 K) separates the TPC from other components. The LXe (and the HFE7000 fluid) is held at 147 kPa (1100 torr) and 167 K, with possible temperature variations $< \pm 0.1$ K, by cooling the inner vessel of the cryostat with a closed circuit refrigerator. The cryostat is vacuum insulated and has a total radial thickness of 5 cm of low-background copper. It is further encased in a 25 cm thick low-activity lead shield. Signals from wire triplets, spaced 9 mm from each other, and LAAPDs are brought out of the cryostat and lead shield, where they are amplified, shaped, and digitized at 1 MS/s by room temperature electronics. The detector infrastructure includes a gas phase recirculation system consisting of a boiler, a pump, a hot Zr purifier, gas purity monitors [14], and a condenser. A substantial control system maintains a very small (< 85 torr) pressure difference across the TPC vessel that is built out of 1.37 mm thin copper to keep backgrounds low. A calibration system allows the insertion of miniaturized radioactive sources to various positions immediately outside of the TPC.

The clean room module housing the cryostat and the TPC is surrounded on four sides by an array of 50 mm thick plastic scintillator panels [15]. The array detects muons traversing the lead shielding with an efficiency of 95.9%. EXO-200 is located at a depth of about 1600 mwe in a salt deposit of the Waste Isolation Pilot Plant, near Carlsbad, New Mexico. The muon flux at this site was measured [16] to be 3.1×10^{-7} s^{-1} cm^{-2} sr^{-1}. A paper describing the EXO-200 detector in detail is in preparation.

For the data presented here, EXO-200 was filled with ~175 kg of xenon enriched to 80.6 ± 0.1% in the isotope 136 (^{enr}Xe). The remaining fraction (19.4%) is the isotope 134; the rest of the natural Xe isotopes represent negligible contributions. ^{85}Kr is a radioactive fission product with $Q_\beta = 687.1$ keV and $T_{1/2} = 10.8$ yr that has been present in the atmosphere since the nuclear age and generally contaminates Xe, as a trace component of natural Kr. The EXO-200 enriched Xe was measured [17,18] to contain $(25 \pm 3) \times 10^{-12}$ g/g of natural Kr, substantially less than the typical concentration of 10^{-8}–10^{-7} found in Xe after distillation from air.

The data were collected between May 21, 2011 and July 9, 2011, for a total of 752.66 h of low-background running. During the same period, about 2 h of every day were devoted to detector calibration using ^{60}Co and ^{228}Th sources. A specific source was inserted each day at one

out of five ''standard'' positions near the TPC. Typically, a source was used to scan these positions over a week and then replaced with a different one. Data analysis is performed by two independent groups, providing cross-checks of the results. The detector calibration procedure begins by fitting the energy spectra from the sources to obtain an electron lifetime (τ_e) in the LXe and an overall correspondence between the charge and the energy deposited in the detector. After an initial phase of recirculation of the Xe, τ_e reached 250 μs and it remained between 210 and 280 μs in the data set used here (the maximum drift time at the field used here is $\sim$100 μs). τ_e values are obtained by minimizing the energy resolution for source calibration events, occurring at locations randomly distributed over the entire LXe volume. The dispersion in the τ_e measurements is incorporated in the systematic uncertainty. The daily calibration schedule makes it possible to track and correct for changes in τ_e.

For this initial analysis only, the ionization signal is used to measure the energy. The scintillation signals recorded by the LAAPDs are used to establish the time of the event, identify α particles by their higher light-to-charge ratio compared to electronlike events, and measure α energies. The combined use of scintillation and ionization, to obtain the best energy resolution, is under development.

The ability of the TPC to reconstruct energy depositions in space is used to remove interactions at the detector edges where the background is higher. It also discriminates between single-cluster depositions, characteristic of $\beta\beta$ and single β decays in the bulk of the Xe, from multicluster ones, generally due to γ rays that constitute the majority of the background. In the present analysis, such discrimination employs only one spatial coordinate ($\approx$ 15 mm separation) and the time coordinate ($\approx$ 17 mm separation). The fiducial volume used here contains 63 kg of $^{\mathrm{enr}}$Xe (2.26×10^{26} ^{136}Xe atoms). The detector simulation, based on GEANT4 [19], reproduces the energy spectra taken with calibration sources well. This also applies to the single- to multicluster assignment obtained with the external calibration sources, as illustrated in Fig. 2 for the case of ^{228}Th.

Four full absorption γ calibration peaks, spanning the energy region of interest for this analysis, are derived from the ^{60}Co and ^{228}Th sources: 1173, 1332, 2615, and 511 keV (annihilation radiation). The three high energy γ's provide both single-cluster and multiple-cluster event samples. The energy scale is found to be slightly ($\sim$ 4%) different in the two samples because of the nonzero charge collection threshold on individual wire triplets. An additional calibration energy at 1592 keV is provided by selecting ionization sites produced by e^+e^- pairs from the highest energy γ's. The nature of these energy depositions, however, is different from the others, being produced directly by ionization in a smaller volume. This type of deposition is analogous to that expected from $\beta\beta$ decay and is found to be slightly different from single-cluster depositions from

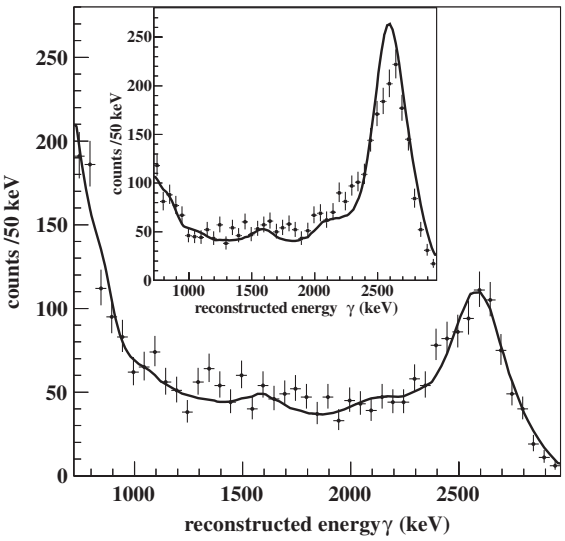

FIG. 2. Energy spectrum for a ^{228}Th calibration source at the midplane of the TPC, 3 cm outside the LXe volume. The intensity (vertical scale) is not fit: The agreement between the Monte Carlo calculations (solid line) and the data tests the accuracy of the simulation against the absolute, National Institute of Standards and Technology traceable, source activity. The energy scale (horizontal axis) has been corrected for τ_e at the time of collection and has had separate energy calibrations applied for single- (main plot) and multiple-cluster (inset) interactions.

γ's. This shift is well reproduced by the simulation, once induction between neighboring wire triplets and other electronics effects are taken into account. After correcting for these two shifts and the (slowly) time-varying τ_e, the energy scale fits well to a linear function. The fractional residuals from this process are shown in the top panel of Fig. 3.

The measured energy resolution is $\sigma_E = 4.5\%$ at 2615 keV. A parameterization of the resolution function is incorporated into the simulation, as shown in the bottom panel of Fig. 3. The analysis uses an energy threshold of 720 keV, chosen so that both the trigger and event reconstruction are fully efficient. Probability distribution functions for each source and position are generated by means of Monte Carlo simulation and compared to the single- and multiple-cluster data (see Fig. 2). This procedure reproduces the activities of the external calibration γ sources to within $\pm$8% of their known activities.

The data collected during low-background running require only two selection cuts to remove modest backgrounds. Cosmic-ray induced backgrounds are rejected by removing events preceded by a veto counter hit in a 5 ms window. This cut removes 124 events introducing a dead time of 0.12%. The decay rate of ^{222}Rn is independently determined to be 4.5 ± 0.5 μBq kg^{-1} from an α-spectroscopy analysis performed by using only scintillation signals, consistent with β-α and α-α time coincidence analyses. Similarly, ^{220}Rn is constrained to

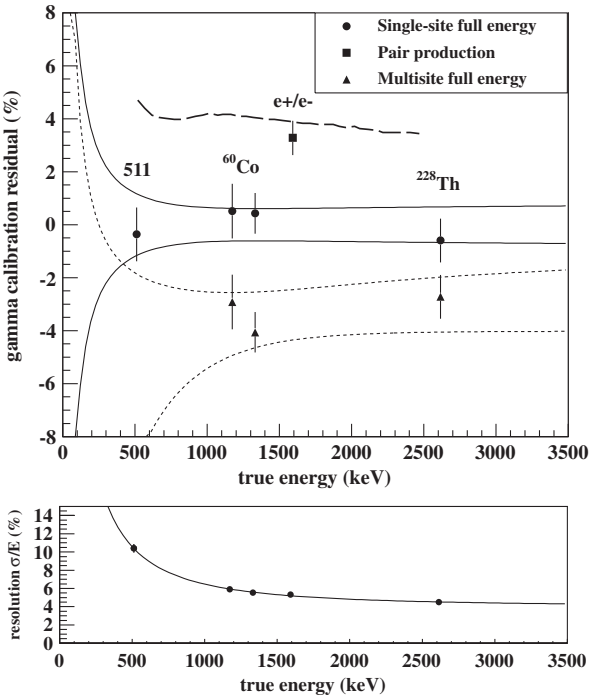

FIG. 3. Top: Fractional residuals between the energy calibration points and the linear model discussed in the text. The single- (solid line) and multicluster (dotted line) uncertainty bands are systematic, stemming from the finite accuracy of the position reconstruction and the τ_e correction. The thick dashed line represents the central value of the shift predicted by the simulation for pointlike energy depositions. Bottom: Measured energy resolution (points) along with a parameterization (line).

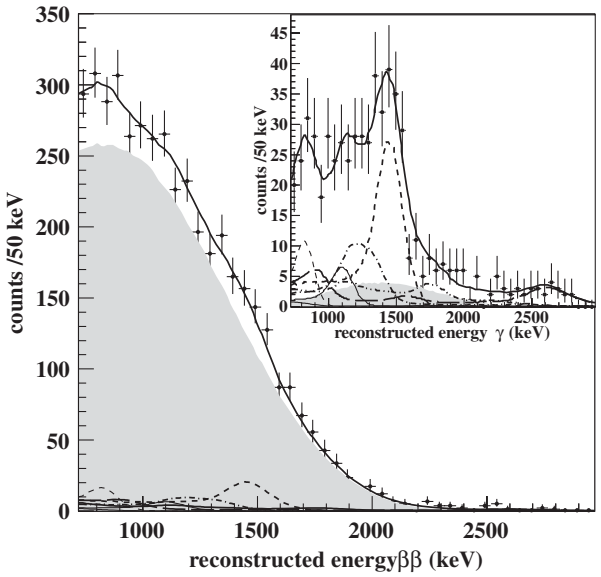

FIG. 4. Energy distributions from 752.66 h of EXO-200 single-cluster events (main panel) and multicluster events (inset). The result of a likelihood fit to a model including the $2\nu\beta\beta$ decay and several backgrounds is shown (solid line) along with the $2\nu\beta\beta$ component (shaded region) and some prominent background components at the radius of the TPC vessel (^{232}Th, long dashed line; ^{40}K, dashed line; ^{60}Co, dash-dotted line; ^{54}Mn, thin dashed line; ^{65}Zn, thin solid line; ^{238}U chain in equilibrium, dash-double-dotted line). Other background components fitting to negligible amounts are not shown, for clarity. The energy scale used for the main panel is consistent with that of single-cluster, β-like events, while the scale of the inset is consistent with the multicluster events it represents. The combined χ^2/degrees of freedom between the model and the data for the two binned distributions shown here is 85/90.

<0.04 μBq kg^{-1} (90% C.L.). In the data set, 72 β-α coincidences are removed. The implementation of this cut introduces a 6.3% dead time due to spurious ionization or scintillation signals. Events are then classified as single- or multicluster and energy spectra are obtained for these two classes, as shown in Fig. 4. The spectra are simultaneously fit to probability distribution functions for the $2\nu\beta\beta$ decay signal (65% of which is above threshold) and various backgrounds by using an unbinned maximum likelihood method. The $2\nu\beta\beta$ probability distribution function is produced by using the Fermi function calculation given in Ref. [20]. The detector simulation predicts a small fraction of the $2\nu\beta\beta$ decay signal to be classified as the multicluster type because of bremsstrahlung as well as charge collection effects. Background models are developed for various components of the detector, inspired by screening of materials performed at the time of the detector's construction and by estimated cosmogenic activation. As Fig. 4 illustrates, the backgrounds involving γ rays are readily identified by their clear multicluster signature, while the single-cluster spectrum is dominated by a large structure with a shape consistent with the $2\nu\beta\beta$ decay of ^{136}Xe. The simultaneous likelihood fit to the single- and multicluster spectra reports a strong signal from the $2\nu\beta\beta$ decay (3886 events) and a dominant contamination from ^{40}K at the location of the TPC vessel (385 events). Other contributions account for a total of less than 650 events, each with a very low significance in the fit. These levels of contamination are consistent with the material screening measurements [12]. By taking only the single-cluster events into account, the signal-to-background ratio is 9.4 to 1.

The α-spectroscopy analysis is used to bound any ^{238}U contamination in the bulk LXe. This is important because ^{238}U decays are followed (with an average delay of $\sim$35 d) by ^{234m}Pa decays, producing β's with a Q value of 2195 keV. The α scintillation spectrum is calibrated by using the lines observed from the ^{222}Rn chain, obtaining a limit for ^{238}U (and ^{234m}Pa) of <10 counts for the data set shown in Fig. 4. In addition, a study of the production of fast neutrons resulting in recoils and captures in the LXe as well as thermal neutrons resulting in captures is used to bound these backgrounds to <10 events for the data set in the figure.

The measured half-life of the $2\nu\beta\beta$ decay in ^{136}Xe obtained by the likelihood fit is $T_{1/2} = 2.11 \pm 0.04(\text{stat}) \pm 0.21(\text{syst}) \times 10^{21}$ yr, where the systematic uncertainty includes contributions from the energy calibration

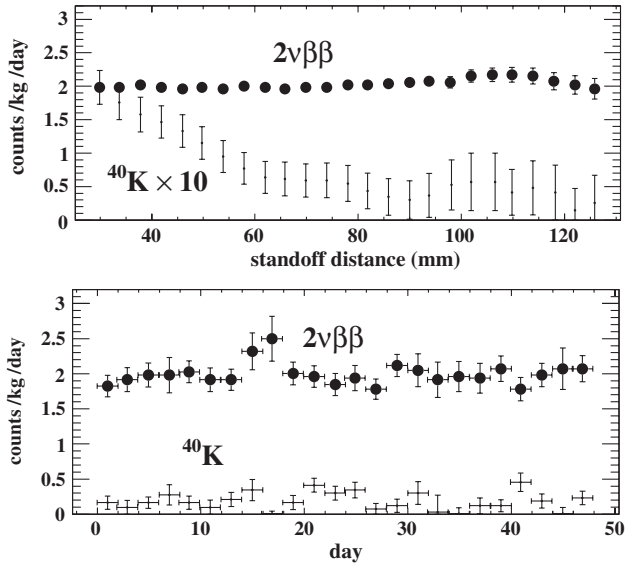

FIG. 5. Top: Measured $2\nu\beta\beta$ decay rate of ^{136}Xe (large points) and largest background contribution (^{40}K, small points) as a function of the standoff distance from detector components. Bottom: Event rates of $2\nu\beta\beta$ and ^{40}K decays as a function of time.

(1.8%), multiplicity assignment (3.0%), fiducial volume (9.3%), and γ background models (0.6%), added in quadrature. The uncertainty from the energy calibration is estimated by using a Monte Carlo method scanning calibration constants within the range illustrated in Fig. 3 and refitting the spectra, weighting the fit results by their likelihood value. The same method is used to quantify the effect of the multiplicity assignment. The fiducial volume uncertainty is determined from the fidelity with which calibration events are reconstructed within a chosen volume as compared to simulation. The γ background model uncertainty is derived from the results of likelihood fits performed with a variety of different background hypotheses.

In Fig. 5, the fitted values of the $2\nu\beta\beta$ and the ^{40}K background are shown as functions of the event standoff distance from materials other than the LXe (top panel) and time in the run. While the ^{40}K is attenuated by the LXe as expected, the $2\nu\beta\beta$ signal appears to be uniformly distributed in the detector and constant in time.

An exhaustive search for β emitters with no γ's, $T_{1/2} >$ 2 days, and energies of interest yields only two candidates: ^{90}Y (supported by ^{90}Sr) and ^{188}Re (supported by ^{188}W). It appears *a priori* unlikely that the bulk of the LXe is uniformly contaminated with these isotopes while simultaneously not showing significant evidence for more common metallic contaminants such as those from the ^{238}U decay chain. Nevertheless, additional test fits are performed by incorporating each isotope separately. At 90% C.L. the $2\nu\beta\beta$ rate is reduced by less than 7% (30%) for the inclusion of ^{90}Y (^{188}Re).

In conclusion, the initial data taking of EXO-200 has provided a clear detection of the $2\nu\beta\beta$ decay in ^{136}Xe. The measured $T_{1/2}$ is significantly lower than the lower limits quoted in Ref. [8] and translates to a nuclear matrix element of 0.019 MeV^{-1}, the smallest measured among the $2\nu\beta\beta$ emitters.

EXO-200 is supported by DOE and NSF in the United States, NSERC in Canada, SNF in Switzerland, and RFBR in Russia. The Collaboration gratefully acknowledges the hospitality of WIPP.

*Now at Department of Radiation Oncology, Stanford University, Stanford, CA, USA.
†Corresponding author.
psbarbea@stanford.edu
‡Permanent address: Istituto Nazionale di Fisica Nucleare, sezione di Padova, Padova, Italy.
§Now at Argonne National Lab, Argonne, IL, USA.
‖Now at Physics Department, Carleton University, Ottawa, Ontario, Canada.
¶Now at Tesla Motors, Palo Alto, CA, USA.
**Now at the Haute Ecole d'Ingénierie et de Gestion, Yverdon-les-Bains, Switzerland.
††Also TRIUMF, Vancouver, British Columbia, Canada.
‡‡Now at the Department of Physics, MIT, Cambridge, MA, USA.

[1] M. Goeppert-Mayer, Phys. Rev. **48**, 512 (1935).
[2] E. Majorana, Nuovo Cimento **14**, 171 (1937); G. Racah, Nuovo Cimento **14**, 322 (1937).
[3] For instance, J. Bjorken and S. Drell, *Relativistic Quantum Fields* (McGraw-Hill, New York, 1965).
[4] J. Schechter and J. W. F. Valle, Phys. Rev. D **25**, 2951 (1982).
[5] F. Šimkovic *et al.*, Phys. Rev. C **77**, 045503 (2008).
[6] F. T. Avignone III, S. R. Elliott, and J. Engel, Rev. Mod. Phys. **80**, 481 (2008).
[7] K. Nakamura *et al.* (Particle Data Group), J. Phys. G **37**, 075021 (2010).
[8] R. Bernabei *et al.*, Phys. Lett. B **546**, 23 (2002); Yu. M. Gavriljuk *et al.*, Phys. At. Nucl. **69**, 2129 (2006).
[9] M. Redshaw *et al.*, Phys. Rev. Lett. **98**, 053003 (2007).
[10] H. Drumm *et al.*, Nucl. Instrum. Methods **176**, 333 (1980).
[11] R. Neilson *et al.*, Nucl. Instrum. Methods Phys. Res., Sect. A **608**, 68 (2009).
[12] D. Leonard *et al.*, Nucl. Instrum. Methods Phys. Res., Sect. A **591**, 490 (2008).
[13] 3M, see http://solutions.3m.com.
[14] A. Dobi *et al.*, arXiv:1106.1812 [Nucl. Instrum. Methods (to be published)].
[15] Provided by the KARMEN Collaboration.
[16] E. I. Esch *et al.*, Nucl. Instrum. Methods Phys. Res., Sect. A **538**, 516 (2005).
[17] A. Dobi *et al.*, arXiv:1103.2714.
[18] A. Dobi *et al.*, arXiv:1109.1046.
[19] S. Agostinelli *et al.*, Nucl. Instrum. Methods Phys. Res., Sect. A **506**, 250 (2003).
[20] G. K. Schenter and P. Vogel, Nucl. Sci. Eng. **83**, 393 (1983).